Published in

Journal of Atmospheric and Solar-Terrestrial Physics,

240, 105959, doi.org/10.1016/j.jastp.2022.105959, 2022

Studies of noctilucent clouds from the stratosphere during the SONC balloon-borne experiment in 2021

P. Dalin[a,b], H. Suzuki[c], N. Pertsev[d], V. Perminov[d], D. Efremov[e,f], P. Voelger[a], V.L. Narayanan[g,h], I. Mann[g], I. Häggström[i], M. Zalcik[j], O. Ugolnikov[b], J. Hedin[k], J. Gumbel[k], R. Latteck[l], G. Baumgarten[l]

[a] Swedish Institute of Space Physics (IRF), Kiruna, Sweden
[b] Space Research Institute RAS, Moscow, Russia
[c] Meiji University, Kawasaki, Japan
[d] A.M. Obukhov Institute of Atmospheric Physics RAS, Moscow Russia
[e] Aerospace Laboratory ñStratonauticaò, Moscow, Russia
[f] M.V. Lomonosov Moscow State University, Moscow, Russia
[g] UiT the Arctic University of Norway, Tromsø, Norway
[h] Department of Electronic and Electrical Engineering, University of Bath, Bath, United Kingdom
[i] EISCAT Scientific Association, Kiruna, Sweden
[j] NLC CAN AM, 1005-11230 St. Albert Trail, Edmonton, AB T5M 3P2
[k] Department of Meteorology (MISU), Stockholm University, Stockholm, Sweden
[l] Leibniz Institute of Atmospheric Physics, Rostock University, Kühlungsborn, Germany

Abstract

On the night 16-17 August 2021, a balloon-borne experiment called Stratospheric Observations of Noctilucent Clouds (SONC) was successfully performed. A big scientific balloon, having onboard three automated cameras for studies of noctilucent clouds (NLC), was launched to 32.7 km altitude from Esrange (northern Sweden). All three NLC cameras and electronics were completely operational in the stratosphere for more than 10 hours at low temperatures of about ï 30°C. Two wide angle cameras registered an extended NLC field of about 1700 km long in the twilight sky sector from the north-west to the north-east of Esrange. NLC were of a moderate brightness and were located at high latitudes between 68° and 71°N. The NLC field was located in a cold area (138ï 142 K) below the frost point temperature (145ï 148 K) in the mesopause region that was confirmed by Aura/MLS satellite and Esrange lidar measurements. The balloon-borne NLC measurements were accompanied by ground-based lidar and radar measurements. The latter have registered Polar Mesosphere Summer Echoes (PMSE) in the same volume of the summer mesopause along with NLC observed from the stratosphere that has been performed for the first time above northern Scandinavia. We describe the technique and method of the NLC observation from the stratosphere as well as present the first scientific results of the SONC experiment.

Keywords: noctilucent clouds, balloon-borne stratospheric observations, mesospheric dynamics, atmospheric gravity waves

Highlights:

1. Balloon experiment was successfully realized to study NLC from the stratosphere
2. NLC field had horizontal scales of about 1700 km long from east to west
3. NLC and PMSE were simultaneously observed in a common mesopause volume
4. NLC field was located in a cold area of the mesopause

1. Introduction

Noctilucent clouds (NLC) are the highest clouds in the Earthôs atmosphere. They can be observed in the summer mesopause region between 80 and 90 km altitude at middle and polar latitudes of both hemispheres. NLC are composed of water-ice particles of 30ï 100 nm in radius that scatter sunlight and thus the clouds are observed against the dark twilight arc from May until September in the Northern Hemisphere and from November to February in the Southern Hemisphere (Bronshten and Grishin, 1970; Gadsden and Schröder, 1989; Liu et al., 2016). NLC have also been observed from space and in this case they are usually called Polar Mesospheric Clouds (PMC) (Thomas, 1984).

Noctilucent clouds often exhibit a wave structure due to a complex interplay between small-scale turbulence processes of 10-1000 metres, atmospheric gravity waves (GW) with wavelengths of 10-1000 km, planetary waves, solar thermal tides and lunar gravitational tides of about 10000 km wavelength (Witt, 1962; Fritts et al., 1993; Rapp et al., 2002; Kirkwood and Stebel, 2003; Chandran et al., 2009; Dalin et al., 2010; Fiedler et al., 2011; Taylor et al., 2011; Pertsev et al., 2015). Sometimes, distinct non-linear mesospheric phenomena like mesospheric fronts can be found with temperature gradients of 20-25 K over a few km, clearly separating two volumes of the mesopause having cold and warm air masses (Dubietis et al., 2011; Dalin et al., 2013; Thurairajah et al., 2021).

NLC/PMC are systematically studied from the ground by means of optical imagers and lidars as well as from space using dedicated satellites and instruments (The Aeronomy of the Ice in the Mesosphere (AIM), Odin, Solar Backscatter Ultraviolet Radiometer (SBUV) instruments) (e.g., Karlsson and Gumbel, 2005; Dalin et al., 2008; Bailey et al., 2009; Fiedler et al., 2011; DeLand and Thomas, 2015). Additionally, irregular (campaign-based) NLC observations have been conducted by using sounding rockets and aircraft (Zadorozhny et al., 1993; Gumbel and Witt, 2001; Reimuller et al., 2011; Suzuki et al., 2022). All of these techniques have both advantages and disadvantages. In particular, ground-based measurements provide a high horizontal resolution of ~20 m and high temporal resolution of ~1 second using optical NLC imagers (Dalin et al., 2010; Baumgarten and Fritts, 2014) as well as high vertical resolution of 50-150 metres using lidars (Baumgarten et al., 2009) but are limited by tropospheric weather conditions and are restricted to a certain small region above the Earthôs surface. Satellite measurements, on the other hand, provide global PMC coverage, but have low spatial horizontal resolution (~1 km) and low temporal resolution of several minutes. Additionally, they have large spatial measurement gaps of several hundreds of km between adjacent orbits at middle and subpolar latitudes (45-60°N) due to a spacecraft orbiting the Earth. Thus, there is no perfect technique to observe and study microphysical and dynamical processes of NLC/PMC so far.

Propagating gravity waves induce dynamical and microphysical changes in the NLC genesis, evolution and their optical properties, which have been intensively studied with model simulations (i.e., Witt, 1962; Turco et al., 1982; Jensen and Thomas, 1994; Klostermeyer, 1998; Rapp et al., 2002; Fritts et al., 2014; Dong et al., 2021). The main mechanism provides changes in the particle size distribution by a propagating wave due to ice sublimation / condensation. In general, microphysical models (Turco et al., 1982; Jensen and Thomas, 1994; Rapp et al., 2002) demonstrate that gravity waves with periods less than a few hours tend to decrease the size of ice particles, whereas waves with periods more than 6.5 h tend to amplify NLC due to a sufficient growth of ice particles in a cold phase of a wave. However, model simulations made for short-period waves (Shevchuk et al., 2020) show that such waves can provide wavelike patterns of more bright crests and less bright wave troughs due to a wave modulation of an NLC layer without notable changes in sizes of ice particles and in their number density.

At the same time, balloon-borne observations made from stratospheric altitudes (25-40 km) have a potential for comprehensive studies of NLC on a regular basis. Among others, observations from the stratosphere have the following advantages: no dependence on tropospheric weather conditions, the closest location to an NLC layer compared to ground and space observations (making the highest possible spatial resolution from the stratosphere), observing NLC both at very large scales up to 2500 km (due to the Earthꞌs curvature) and at very small scales down to 5 metres. A balloon being located above the highest ozone concentration (between 20 and 25 km at high latitudes) provides NLC observations almost free from ozone absorption in the Chappuis absorption of the scattered light between 400 and 650 nm as it has to travel a long path through the Earthꞌs atmosphere when observing NLC in the twilight sky.

So far, there have been conducted three experiments providing NLC observations from stratospheric balloons (Miller et al., 2015; Dalin et al., 2019, 2020; Fritts et al., 2019). These experiments have provided unique materials for studies of both large-scale and small-scale wave dynamics and turbulent processes in NLC layers. In the present paper, we report on a new balloon-borne experiment dedicated to studies of wave processes in NLC as well as microphysical properties of ice particles in the high latitude mesopause region. We describe the technique, methods of NLC observations from the stratosphere and present first scientific results of this balloon-borne experiment. The stratospheric measurements were accompanied by lidar and radar measurements from the ground in the vicinity to the balloon trajectory. We also use Aura/MLS satellite water and temperature measurements to analyze the environment situation in the mesopause region during the experiment.

2. Technique and method

2.1. Technical characteristics of the imager

The Stratospheric Observations of Noctilucent Clouds (SONC) experiment is a scientific balloon-borne experiment dedicated to studies of large-scale (30 ï 2500 km) and small-scale atmospheric dynamics (5 m ï 30 km) in the summer mesopause as well as microphysics of NLC ice particles. In order to achieve these goals, three high-resolution, high-sensitivity cameras (Sony Ŭ7 Mark III), having a full frame size of 35 mm and 24 megapixel sensor (6000 x 4000 pixels), are utilized. Two cameras are equipped with wide-angle lens (field of view (FoV) is 105.4° x 81.8°) while one camera is fitted with a narrow-angle lens having a FoV of 15.0° x 10.1°. This combination of two wide-angle cameras and one narrow-angle camera yields on the one hand, the horizontal coverage of 180° allowing observing NLC at large scales up to 2500 km in the mesopause, and, on another hand, provides very high horizontal resolution of ~6 m when looking at 83 km from 33 km altitude at elevation angle of 35°. Note that this unique combination is impossible to achieve currently when observing NLC from either the ground or space. These three SONC cameras comprise the SONC imager shown in Fig.1 and its characteristics are presented in Table 1.

Table 1. Technical characteristics of the SONC imager composed of two wide-angle Sony Ŭ7 Mark III cameras and one narrow-angle Sony Ŭ7 Mark III camera.

	Field of view and focal length	Sensor type and size, pixels	Bit depth, image format	Spatial resolution at 83 km as seen from 33 km at 35° elevation angle
Wide-angle camera	105.4° x 81.8° 14 mm	CMOS 6000 x 4000	14 raw	63 m
Narrow-angle camera	15.0° x 10.1° 135 mm	CMOS 6000 x 4000	14 raw	6 m

The performance of the cameras was tested in a thermal chamber at the Swedish Institute of Space Physics (IRF-Kiruna) before the balloon launch. The thermal tests demonstrated that the cameras can operate in a stable way for 24 hours at temperatures between ï 50° and +50°C, which is sufficient for the cameras to operate in the troposphere-stratospheric environment. The electronic unit (developed by Aerospace laboratory ñStratonauticaò in Moscow, Russia) distributes the power to all cameras and controls synchronous operation of all three cameras during the whole balloon flight. This high time resolution allows estimating temporal evolution of small-scale waves and turbulent structures in the NLC layer. The optical axes of two wide-angle cameras are inclined at 36° to the horizontal plane in order to avoid registering the Earthôs surface below (along with bright tropospheric clouds) and bright balloon envelope above. The optical axis of the narrow-angle camera is inclined at 35° to the horizontal plane in order to resolve fine structures of noctilucent clouds with a horizontal resolution of about 6 m. All images are stored on two SD cards (512 GB each) in each camera.

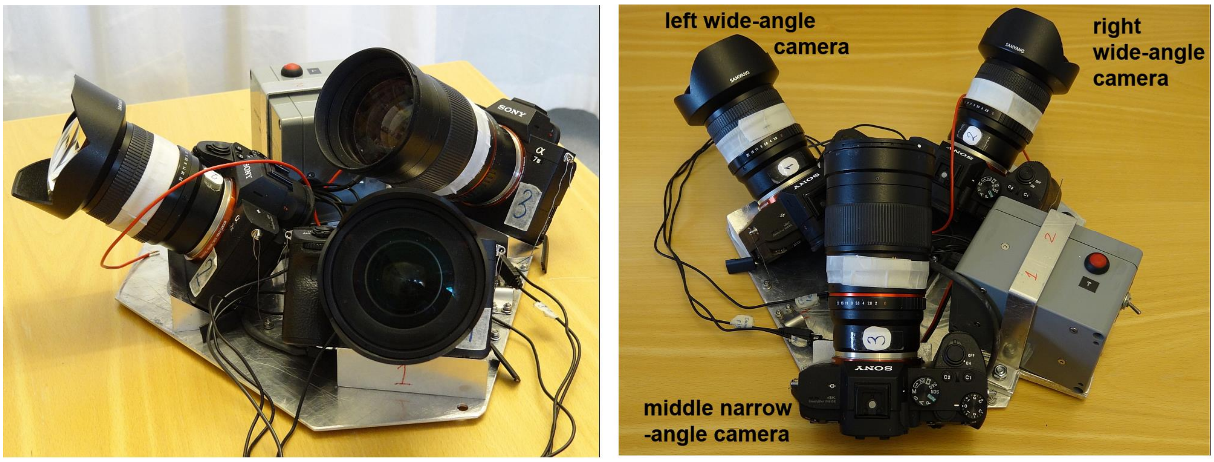

Figure 1. The SONC instrument is composed of three SONY Ŭ7 Mark III cameras and the electronic unit (the grey box with the red button), which was used for observing noctilucent clouds on the XENON stratospheric balloon on the night 16-17 August 2021. Two cameras are equipped with wide-angle lenses and one camera has a narrow-angle lens (located in between two wide-angle cameras).

2.2. The technical characteristics of the balloon experiment

HEMERA is a balloon infrastructure project, funded by the European Commission within its programme the Horizon 2020 (https://www.hemera-h2020.eu/). The project is coordinated by the French space agency CNES and involves a consortium of 13 partners from six European countries and Canada. The HEMERA project offers free of charge balloon flights to the user community. Zero Pressure Balloons (ZPB), each carrying around 150 kg of payload, are launched from either Esrange (Sweden) or Timmins (Canada).

The 2020 balloon campaign KLIMAT was unfortunately cancelled due to the global impact of COVID-19 pandemic. It was instead conducted during the summer of 2021.

The SONC experiment was installed on a scientific ZPB called XENON. The XENON balloon has a 3-axis motorized gimbal stabilized platform, with the elevation angle stability of 0.15° as well as the absolute azimuth pointing accuracy of 1° and stability of 10 arcmin around it. This is important for the SONC experiment to constantly examine a potential presence of NLC in the twilight sector of the sky and obtaining high quality images without a smearing effect.

The XENON balloon was launched from Esrange (67.89°N, 21.08°E) at 19:27 UT (21:27 LT) on 16 August 2021. The height and horizontal profiles of the XENON flight are illustrated in Figure 2.

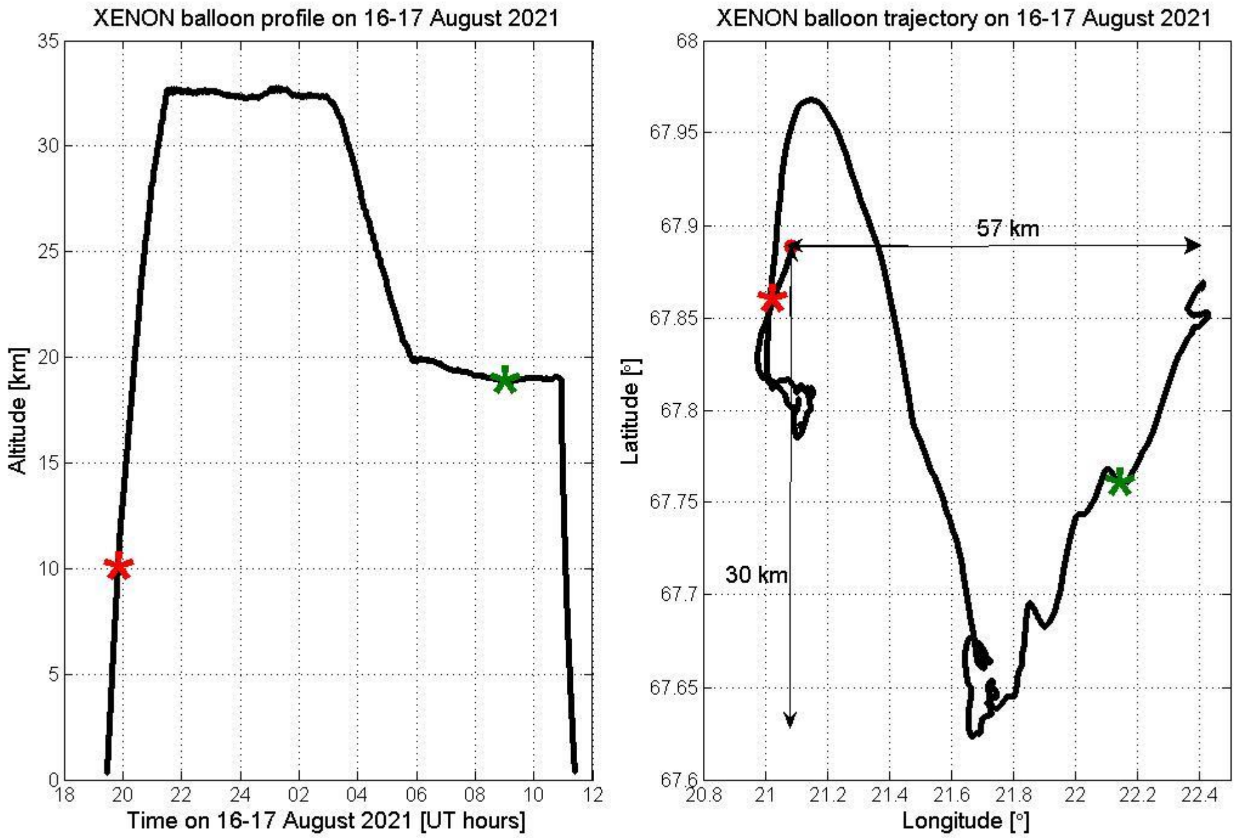

Figure 2. (Left) The XENON balloon height profile on the night 16-17 August 2021. (Right) The horizontal trajectory of the XENON flight. The red dot marks the position of the balloon launch at Esrange. The vertical and horizontal arrows indicate horizontal scales in km. The red and green asterisks on the both panels indicate the start and end of the SONC experiment operation, respectively.

Due to low wind speed in the stratosphere on that night, the XENON balloon was staying rather close to Esrange, at the beginning swinging to the south and north of Esrange and then slowly moving to the southeast and finally to the northeast of Esrange. The travelled distance to the east of Esrange was about 57 km for 16 hours of the flight. The height profile demonstrates a rapid balloon ascent to 32.7 km altitude for 2 hours, the first floating trajectory at about 32.5 km, then the first descent, the second floating trajectory at about 19 km and finally the second rapid descent. The flight height trajectory satisfied different scientific experiments onboard the XENON balloon.

The NLC imager started to operate at 10 km altitude (as planned) at 19:50 UT on 16 August and ended at 09:13 UT on 17 August 2021. The 3D stabilization of the gondola and the NLC imager occurred at 21:35 UT at 32.6 km altitude. There was no telemetry of images to the ground (as designed) but there was a power interface at the CNES control centre which demonstrated the currents supplied by three NLC cameras that was indicative of cameras operation conditions. During the balloon flight in the stratosphere, the temperature varied between ï 30° and ï 32°C. All three cameras and the electronic unit were completely operational without any interruption during the balloon flight. Each camera took images with 6 sec resolution for 13 hours. Automatic exposure bracketing was used to take 5 images in sequence with different exposure times varying between 1/2000 and 2 sec, allowing us to register various NLC brightnesses from very bright to very faint as well as faint and bright stars. This is an important information for the image processing and georeference procedure of the images taken from the stratosphere. For the NLC image analysis, we use two short exposure times (1/250 and 1/30 sec) to minimize the smearing effect due to NLC motion during an exposure time. In total, each camera took about 40,000 images during the flight in the stratosphere.

The landing of the XENON gondola was safe and no payload was damaged. Summarizing, the SONC experiment was successfully realized in the stratosphere, demonstrating its perfect technological performance.

2.3. Image processing

The optical calibration of three SONY cameras, comprising the NLC imager, was performed before the SONC experiment by analyzing reference images of a clear night sky with stars. During the pre-analysis, the camera model was chosen to be described by the 3rd order polynomial. By comparing theoretical horizontal coordinates of reference stars (more than 200 reference stars have been identified in the reference images) with actual horizontal coordinates of reference stars, ten coefficients of the 3rd order polynomial were calculated. These ten coefficients describe all possible distortions in the camera optical path. In other words, relative horizontal coordinates (elevation and azimuth angles relative to the centre of the image) of each pixel in the camera array were calculated. During the balloon flight, about ten reference stars have been identified to find the horizontal coordinates of the centres of the analyzed NLC images of two wide-angle cameras. Then the absolute horizontal coordinates of each pixel were calculated followed by the georeference procedure to project each pixel on the Earth's surface. For this, the mean NLC altitude of 85 km was chosen as will be discussed below. Detailed information on the optical calibration, georeference procedure and error analysis can be found in Dalin et al. (2015).

The gravity wave analysis (identifying and tracing wave crests in a sequence of images) was manually done by measuring pixel coordinates of well-defined wave crests. Pre-analysis of NLC images was done in order to trace several wave crests as long as possible (at least for 5 minutes) in a sequence of images. Then horizontal wavelengths of gravity waves were estimated using the abovementioned georeference procedure. The NLC motion (mean speed and direction) as the whole was estimated by tracing small-scale features (nodules) in NLC, which are supposed to move together with the prevailing horizontal wind in a given space and time, avoiding the analyzed wave crests.

Absolute calibration of the cameras and flat-field correction of the images have not been done so far since these procedures are not required at the present stage of the image analysis.

3. Results

3.1. NLC imager

A careful inspection of images obtained from the stratosphere has demonstrated the following. Noctilucent clouds were registered between 21:38 UT on 16 August and 00:56 UT on 17 August 2021, with the total duration of 3 hours 18 min. An example of NLC images taken by two wide-angle cameras is shown in Figure 3. The NLC were of moderate brightness and were located at low elevation angles less than 24° as viewed from the balloon horizon. Due to this fact, the narrow-angle camera (pointing to 35° elevation angle) did not register any NLC during the balloon flight, i.e., the NLC were located below the FoV of the narrow-angle camera. On future flights we plan to install a small preview GoPro camera (with data downlink) in order to overview a presence of NLC in the field of view of wide-angle cameras. If NLC would be seen then the gondola and the imager could be azimuthally rotated to capture NLC in the field of view of the narrow-angle camera.

In Figs. 3 and 4, one can see wave structures of various scales in noctilucent clouds. The image analysis has demonstrated that there were prevailing medium-scale gravity waves with horizontal wavelengths of 24.4±1.6 km, 34.3±2.1 km, 51.1±4.6 km and 103.4±6.6 km as well as small-scale waves (billows) with horizontal wavelengths of about 11.1±1.4 km. The billows were observed in the FoV of the left wide-angle camera for a short period of about 15 minutes within larger gravity wave bands. The NLC field as the whole moved to the south-west, with the average observed (ground) speed of 53.4±14.2 m/s and with the average azimuth of 235.6±5.3° (counting clockwise from the north). When calculating NLC velocities, the horizontal velocity of the balloon motion relative to the ground of 4 m/s with the azimuth of 10° was taken into account at times of the analyzed NLC images. The mean NLC altitude was assumed to be equal to 85 km based on lidar and radar measurements as will be demonstrated below. The total visual extension of the observed NLC field was about 1700 km stretching from the west to the east and about 300 km from the north to the south, i.e., the visible part of the NLC field were located between 68°N and 71°N, and between 7°W and 40°E. Detailed studies of the wave dynamics and NLC ice particles microphysics will be addressed in future papers.

In the stratosphere, there were several rotations of the gondola due to various scientific experiments onboard. At the beginning of the NLC observation (21:38 UT), the gondola pointed to the north that corresponds to the pointing direction of the narrow-angle camera of the SONC imager. At 22:37 UT, the gondola was rotated in the north-east direction (60° from the north), allowing us to entirely observed the eastern part of the NLC field. At 23:42 UT, the gondola was rotated in the north-west direction (315° from the north). The rotation actually benefited our experiment: the western part, which was the brightest part of the observed NLC field, demonstrating interesting small-scale dynamics, was completely captured in the field of view of the left wide-angle camera. Because of this, we show three most interesting sequences during the NLC display viewed from the stratosphere in Figure 3: the right-side NLC images were taken by the right wide-angle camera pointing to the north-east (38° from the north), the images in the middle panels were taken by the left wide-angle camera looking to the NNW (20°), and the left-side NLC images were taken by the left wide-angle camera pointing to the WNW (278°) after the rotation of the gondola to the north-west.

It is interesting to note an atmospheric effect caused by the Earth's shadow: on the left-side images of Figure 3 one can see the NLC field located at the edge of the shadow (the dark area in the left part of the left hand side images); in other words, the location of the Earth's shadow limited the observation of the whole field of NLC in this particular area. Figure 5 shows the geospatial projection of the NLC images displayed in Figure 3.

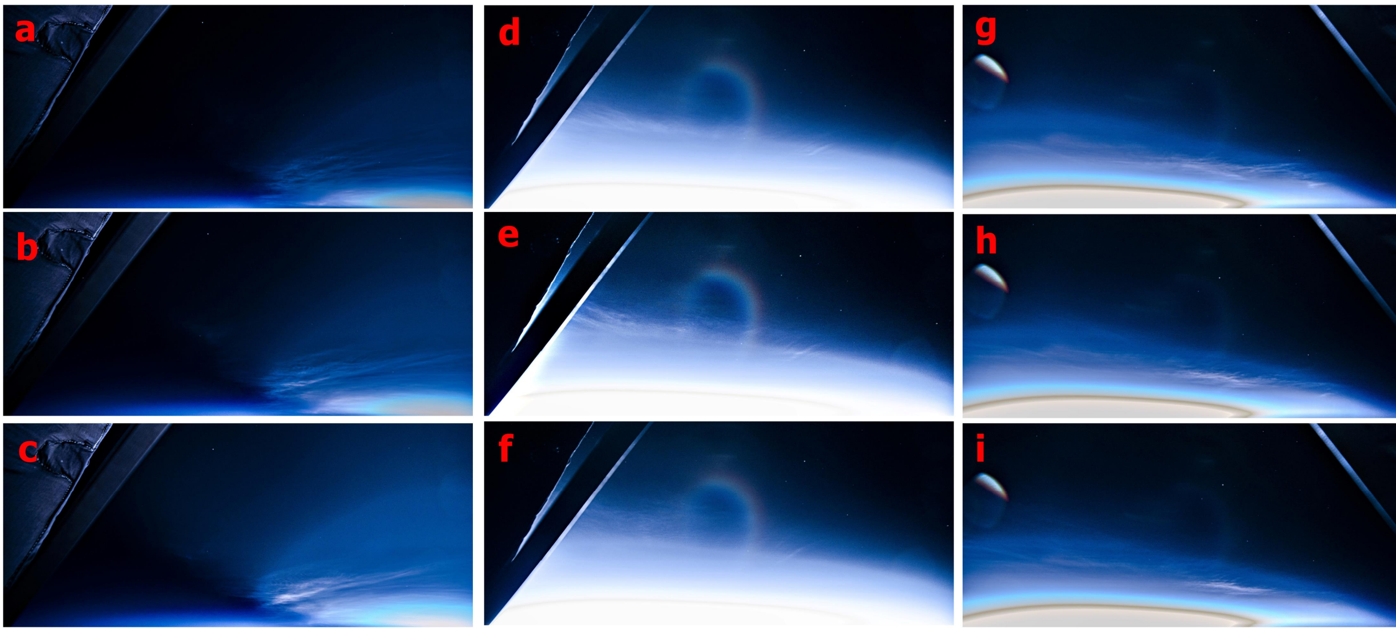

Figure 3. Noctilucent clouds observed from the stratosphere during the SONC balloon-borne experiment on the night 16-17 August 2021. Examples of images of noctilucent clouds taken by two wide-angle cameras of the SONC experiment from the stratosphere at about 32.5 km: Left-panel images were taken at 23:45:41, 23:55:41, 00:05:41 UT by the left wide-angle camera (see Figure 1), pointing to 278° from the north. Middle-panel images were taken at 22:37:13, 22:47:13, 22:57:13 UT by the left wide-angle camera, pointing to 20°. Right-panel images were taken at 22:04:02, 22:14:02, 22:24:07 UT by the right wide-angle camera, pointing to 38° from the north. For the geometry of the cameras the reader is referred to Figure 1.

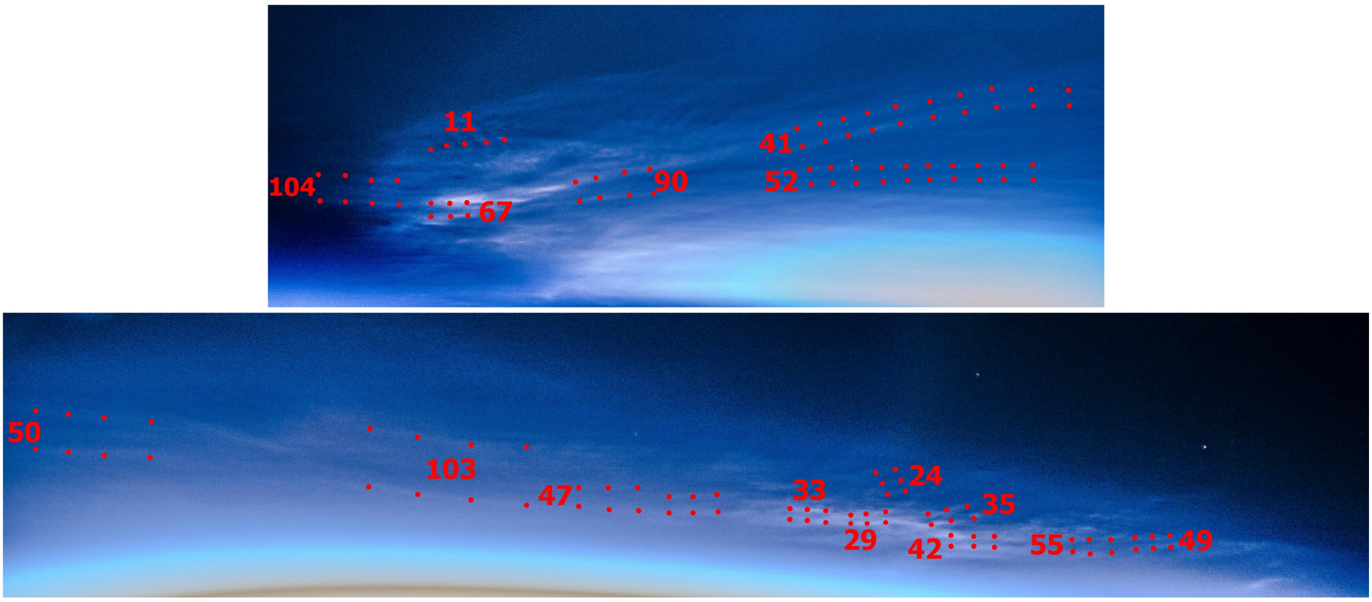

Figure 4. The upper panel is the enlarged part of Figure 3c. The lower panel is the enlarged part of Figure 3g. The dots and corresponding numbers mark gravity wave crests and their horizontal wavelengths in km being analyzed in the paper.

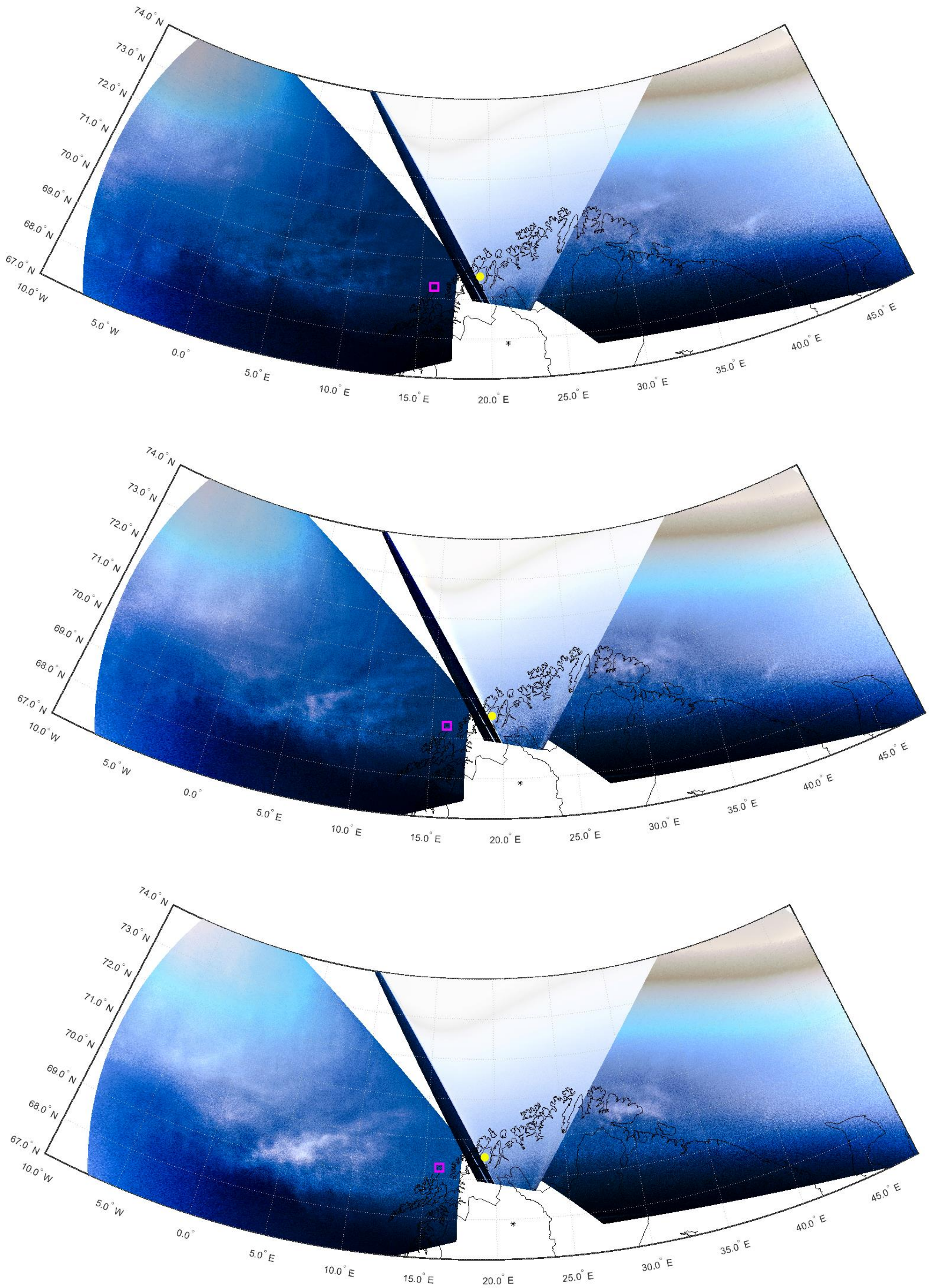

Figure 5. Projection of the images shown in Figure 3 on the Earthôs surface. When projected on the surface, the mean NLC altitude was equal to 85 km. The black asterisk, the magenta square and the yellow dot show the positions of Esrange, Andøya and Tromsø, respectively.

3.2. Lidar and Aura/MLS satellite measurements

During the balloon launch on the night 16-17 August 2021, complementary lidar measurements were performed at Esrange. A Rayleigh/Mie/Raman backscatter lidar was developed by the Bonn University to monitor aerosols in the troposphere, stratosphere and mesosphere as well as to determine temperature profiles in the aerosol-free part of the atmosphere (Blum and Fricke, 2005). We use lidar backscattered signal from the 532-nm wavelength channel to estimate a potential presence of an NLC layer over Esrange and to calculate an atmospheric temperature profile in the mesopause region. The vertical and time resolutions of the obtained measurements are 150 m and 4.2 min, respectively.

The results of the lidar measurements are shown in Figure 6. The left panel of Fig. 6 illustrates the lidar count data profile integrated over 2 hours (between 22:30 and 00:30 UT) when the NLC observed from stratosphere had their highest elevation angles, i.e., closest position to Esrange. One can see two small but defined peaks in the lidar count profile at 84 km and 86 km (marked with the red arrows) which might be attributed to the presence of NLC over Esrange. As will be shown below, these lidar peaks are within altitude ranges of polar mesosphere summer echoes registered by two radars. Based on this integrated count profile, a temperature profile has been calculated assuming atmospheric hydrostatic equilibrium. At the upper end of the profile (at 95 km) a seed temperature equal to 140 K was taken from Aura/MLS satellite measurements. The lidar temperature profile, smoothed by using a 1 km running average in height, is shown by the blue line on the right panel of Figure 6. One can see large temperature variations of 15ï 20 K in the mesopause between 84 and 90 km, which were caused by gravity waves having vertical wavelengths of about 2 km. Similar temperature disturbances due to gravity waves (10ï 20 K at 85ï 95 km) were measured during summer rocket campaigns conducted at Andøya (Rapp et al., 2002).

The Aura/MLS temperature and water vapor measurements have been used to order to obtain a comprehensive picture of the mesopause environment in the region of the NLC observation. Aura/MLS temperature and water vapor measurements of ver.5.0 and level 2 data quality were obtained from the NASA public web-site: https://acdisc.gesdisc.eosdis.nasa.gov/data/Aura_MLS_Level2/. The description on the MLS temperature product and its validation can be found in Froidevaux et al. (2006) and Schwartz et al. (2008). The validation of water vapor data is described in detail by Read et al. (2007) and Lambert et al. (2007).

We have analyzed all available temperature and water vapor profiles in the northern Scandinavia region and selected two profiles of temperature and water vapor closest to the position of Esrange (67.89°N, 21.08°E). Unfortunately, there were no Aura/MLS measurements directly over Esrange but to the north-east of Esrange (68.90°N, 36.66°E) and to the north-west of Esrange (68.90°N, 11.94°E), which are away from Esrange by 648 km and 392 km, respectively. Also, the Aura temperature and water vapor profiles were measured at 00:45 UT (north-east of Esrange) and 02:24 UT (north-west of Esrange) on 17 August 2021, which are outside the integrated lidar temperature measurement. These spatial and temporal differences might provide differences in the temperatures as measured from the ground and space. At the same time, the right panel of Figure 6 demonstrates that the temperature profiles show similar mean values between 82 and 88 km, and between 90 and 92 km. The magenta and red profiles are as measured by the Aura/MLS instrument to the north-east and to the north-west of Esrange, respectively. Having low vertical resolution of Aura/MLS measurements of about 10ï 12 km in the mesopause region, the Aura/MLS temperature profiles cannot resolve large temperature variability as measured by the lidar, but their mean values are consistent. The green line is the frost point temperature as calculated from Aura/MLS water vapor data based on thermodynamics of the vapor pressure of ice (Murphy and Koop, 2005). One can see that the lidar temperature (the blue line) was below the frost point temperature (145ï 148 K) between 83.3 and 84.3 km, and between 85.7 and 86.8 km, confirming the principal possibility of the existence of ice particles in these height ranges. At the same time, large variability of the temperature around the freezing point did not allow ice particles to grow to large sizes since ice particles evaporate much quicker in a warm phase of a wave than they grow again in a cold phase on time scales of less than 400 min (Rapp et al., 2002). This led to the formation of smaller ice particles and, as a result, to little backscattered signal peaks registered by the Esrange lidar at 84 km and 86 km.

Note that the ALOMAR lidar (Baumgarten, 2010) located at Andøya (northern Norway) was prepared to conduct measurements in the mesopause during the SONC experiment, but poor weather conditions over Andøya did not allow us to perform the planned lidar measurements.

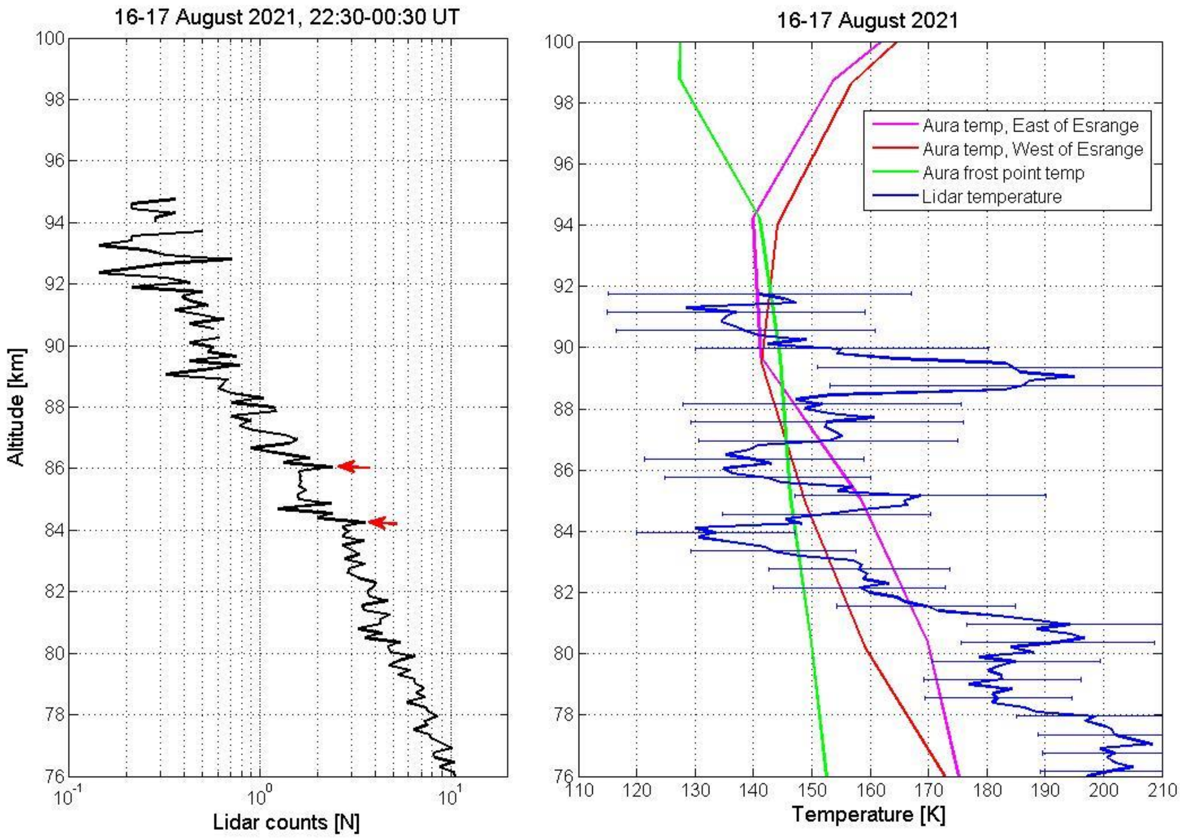

Figure 6. (Left) The lidar count profile integrated over 2 hours from 22:30 UT to 00:30 UT on the night 16-17 August 2021. Two small peaks in the profile which might be attributed to NLC layers are marked with the red arrows. (Right) Temperatures profiles as measured by Aura/MLS spectrometer: the magenta profile is to the north-east of Esrange measured at 00:45 UT, the red profile is to the north-west of Esrange measured at 02:24 UT, the green profile is the Aura frost point temperature estimated from water vapor measurements. The blue profile is the mean Esrange lidar temperature as estimated from the lidar count profile and the blue horizontal bars show uncertainties (1 standard deviation) of the mean temperature profile.

The overview of the temperature situation around the globe is shown in Figure 7, which demonstrates the difference between the actual temperature and the frost point temperature at about 90 km altitude as measured and estimated from Aura/MLS data. Having a low vertical resolution in the mesopause (10ï 12 km), this particular level at about 90 km demonstrated the lowest temperatures on this particular day in a given volume of the mesopause where NLC were observed. These data are shown for 17 August 2021, selecting nighttime measurements only (daytime measurements have been ignored) to obtain the most realistic temperature situation in relation to the observed nighttime NLC display. The red oval shows the observed NLC position as seen from the balloon. We can see that the NLC location fits well to a relatively small area (comparing to global scales) of low temperatures which were below the frost point temperature by 3ï 7 K. This supports the assumption that low temperatures play an important role in the formation of noctilucent clouds in this particular case. Note that the northernmost edge of the observed NLC field was limited by the bright twilight sky at the very horizon.

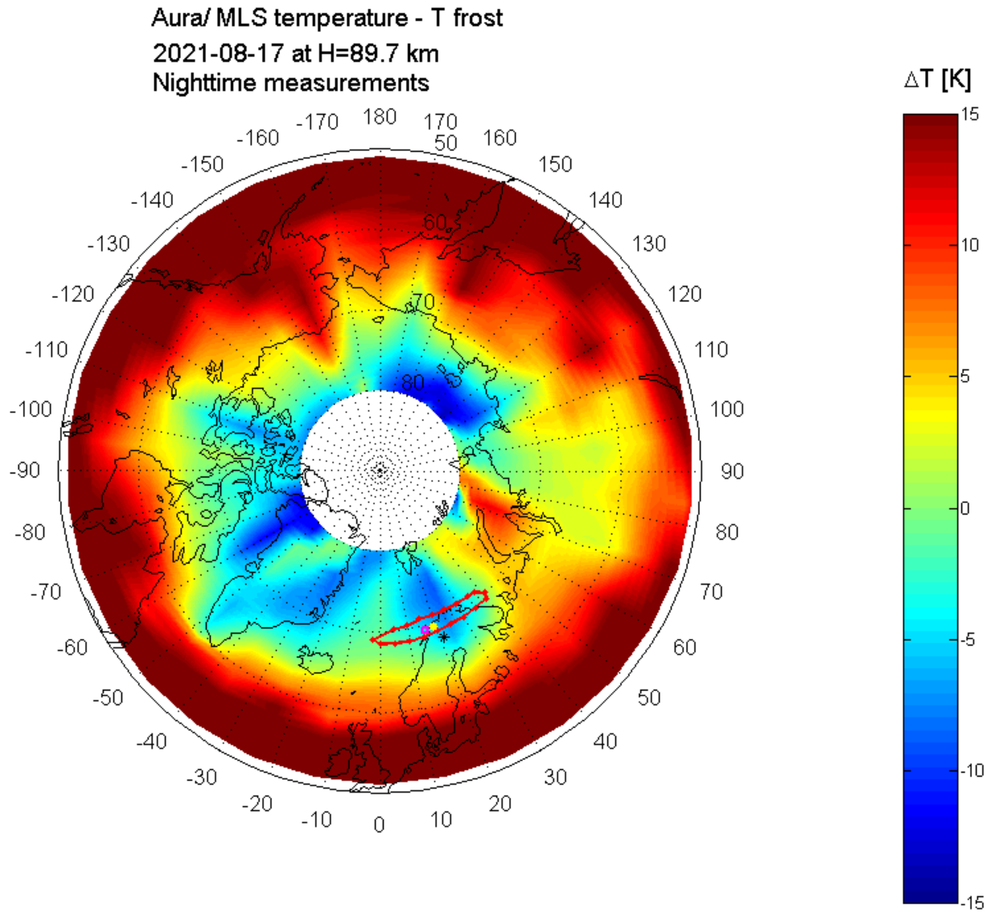

Figure 7. A map of the difference between Aura/MLS temperature and the frost point temperature at about 90 km altitude on 17 August 2021. The blue color code (negative values) means the temperature is below the frost point temperature allowing the existence of ice particles. The red oval shows the location of the NLC field as observed from the stratosphere. The black asterisk, the magenta square and the yellow dot show the positions of Esrange, Andøya and Tromsø, respectively.

3.3. Radar measurements

Complementary radar measurements were performed during the SONC balloon experiment on the night 16-17 August 2021. Two radars were operational during the experiment: EISCAT 224 MHz radar located at Tromsø, northern Norway, and MAARSY 53 MHz located at Andøya, northern Norway (Latteck et al., 2012). These radars are capable of measuring Polar Mesosphere Summer Echoes (PMSE) which are strong radar returned signals. PMSE are induced by the combined effect of a turbulent medium and plasma processes, in which electrically charged aerosols of several nanometer size play a dominating role (Cho and Röttger, 1997; Rapp and Lübken, 2003; Mann et al., 2019; Narayanan et al., 2022).

The results of the MAARSY observation is shown in Figure 8. One can see the clear presence of the PMSE during the stratosphere based NLC observation marked by two red arrows on this plot. The PMSE were mainly located between 83 and 88 km altitude. One can also see progressively downward filaments due to propagating gravity waves (Fritts et al., 1988). Note that the location of MAARSY coincides with the observed NLC field viewed from the stratosphere as shown by the magenta square in Figure 7, i.e., there was a common volume observation of both the PMSE and NLC in the mesopause above Andøya.

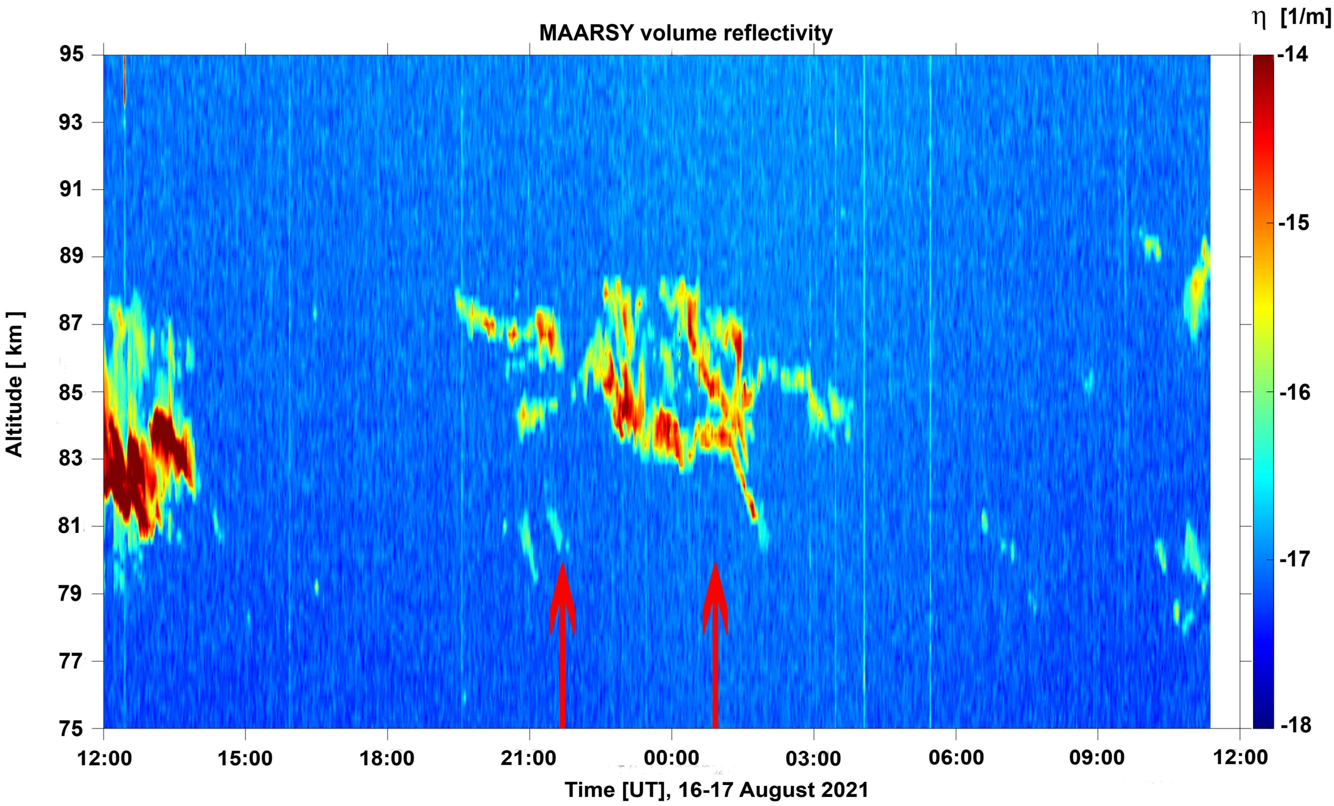

Figure 8. MAARSY 53 MHz measurements of PMSE volume reflectivity above Andøya (69.30°N; 16.04°E) during the SONC balloon experiment on the night 16-17 August 2021. Two red arrows show the beginning and end of the NLC observation from the stratosphere.

The results of the EISCAT 224 MHz radar operation is illustrated in Figure 9, which display the PMSE parameters of radar backscattered peak power of the echoes, Doppler shift and spectral width that were derived following the method described by Mann et al. (2016) and Narayanan et al. (2022). One can see the PMSE layer was located between 85 and 88 km that is consistent with the PMSE registered by MAARSY. Doppler shifts varied from ï 10 to +10 Hz, i.e., approximately within ±7 m/s. Spectral widths were in the range of 2ï 10 Hz that corresponds to typical PMSE spectral widths (Mann et al., 2019; Narayanan et al., 2022). Note that there were intermittent PMSE occurrences throughout the period of the NLC observation that might be explained by temperature variability around the freezing point due to propagating gravity waves as was proposed to explain two weak NLC signals observed in the lidar profile. Besides, PMSE are typically weaker at the 224 MHz EISCAT radar frequency than at the 53 MHz MAARSY frequency. This is because PMSE decrease steeply with increasing frequency. Thus, a comparison of EISCAT VHF and UHF observations shows that the volume reflectivity is inversely proportional to the fourth power of radar frequency (Ge et al., 2020). The location of the EISCAT radar (the antenna was pointing vertically) coincides with the observed stratosphere based NLC field observation as shown by the yellow dot in Figure 7, i.e., there was a common volume observation of both the PMSE and NLC in the mesopause above Tromsø.

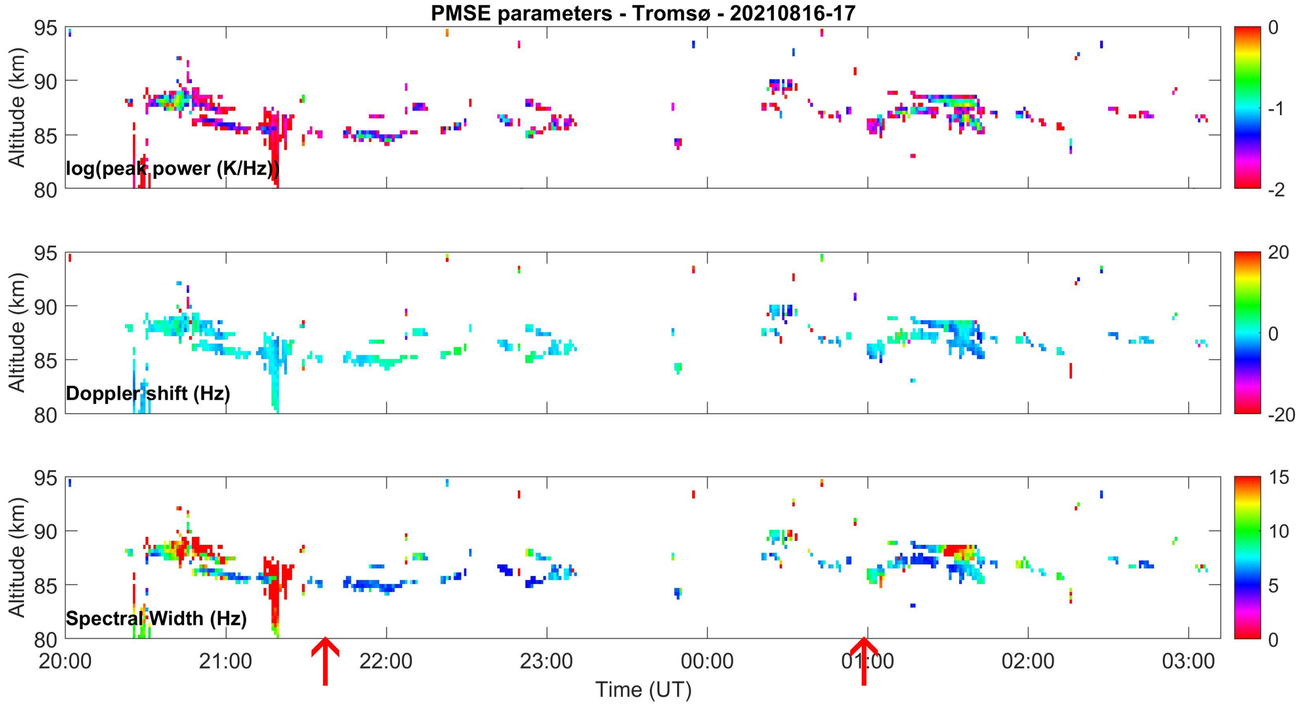

Figure 9. EISCAT 224MHz radar measurements of PMSE parameters above Tromsø (69.58°N; 19.23°E) during the SONC balloon experiment on the night 16-17 August 2021. The upper panel shows the radar power, the middle panel is the Doppler shift and the lower panel illustrates the radar spectral width. Two red arrows show the beginning and end of the NLC observation from the stratosphere.

4. Discussion

The average observed velocity (~53 m/s) with the average azimuth (~236°) of the whole NLC field corresponds well to NLC velocities and wind directions in the summer mesopause at high latitudes (Ludlam, 1957; Witt, 1962; Haurwitz and Fogle, 1969; Gadsden and Schröder, 1989). The observed gravity waves with horizontal wavelengths of about 24, 34, 51 and 103 km (shown in Figure 4) are within the range of the gravity wave spectrum estimated from previous studies (Witt, 1962; Bageston et al., 2009; Chandran et al., 2009; Pautet et al., 2011; Demissie et al., 2014). The observed small-scale gravity waves (billows) with horizontal wavelengths of about 11 km are also within the range of wavelengths for small-scales waves previously studied in noctilucent clouds (Witt, 1962; Haurwitz and Fogle, 1969; Pautet et al., 2011; Baumgarten and Fritts, 2014). The small-scale billows existed for a short period of about 15 minutes which is in the range of typical lifetimes of 6ï 24 minutes for NLC billows (Haurwitz and Fogle, 1969). The observed billows accompanied larger wave band structures and, in this case, billows are thought to be an indication of evolving instability structures generated during larger wave breaking (Fritts et al., 1993; Baumgarten and Fritts, 2014).

It is interesting to compare the observed NLC seen from the stratosphere with those seen by the Aeronomy of Ice in the Mesosphere (AIM) satellite from space (Russell III et al., 2009). We have analyzed Cloud Imaging and Particle Size (CIPS) images (McClintock et al., 2009) available at https://lasp.colorado.edu/aim/browse-images.php?dataset=pmc and found the following orbit strips that were closest in time and space to northern Scandinavia: 78497 at 07:52 UT and 78498 at 09:27 UT on 16 August 2021 as well as 78511 at 06:04 UT, 78512 at 07:39 UT and 78513 at 09:14 UT on 17 August 2021 (all these orbit strips are not shown in the paper). Bright NLC were seen over northern Scandinavia and around it but on the previous day, 16 August, on two orbit strips 78497 and 78498, i.e., 12ï 13 hours before the NLC seen from the balloon. On the orbit strips taken at 06:04, 07:39 and 09:14 UT on 17 August there were no NLC close to the location of the NLC observed from the stratosphere. Thus, the AIM satellite missed the observed NLC due to the difference in the observation times. It means that the NLC had a rather short lifetime of less than 8.4 hours (difference between the NLC start at 21:38 UT on 16 August and no NLC at 06:04 UT on 17 August) and could not be observed by the AIM satellite in this particular case. It is also confirmed by the short period of the NLC visibility (about 3.3 hours) from the stratosphere.

Note that the Swedish Odin satellite was prepared to conduct NLC observations in a special tomographic mode (Karlsson and Gumbel, 2005) above northern Scandinavia during the SONC experiment. However due to a number of issues this planned experiment was not realized.

The NLC particle size distribution (shape of the particle size distribution, mean radius and width) can be estimated based on the color ratio technique using multi-wavelengths of the cameras, i.e., sensor RGB values (von Cossart et al., 1999; Ugolnikov et al., 2017; Ugolnikov, 2021). Also, the color ratio technique provides additional information on the NLC altitude estimation (Ugolnikov, 2021). The advantage of using balloon-borne NLC measurements is that such observation, being conducted above the level of the main ozone concentration (20ï 25 km at high latitudes), provide minimum absorption in the Chappuis absorption bands between 400 and 650 nm as the scattered NLC light travels a long slant path through the Earthôs atmosphere and through the ozone layer as well. At the same time, the Chappuis absorption remains significant if NLC are illuminated by the sunlight having a tangent trajectory passing a long horizontal distance through the ozone layer. The minimum ozone absorption and analysis of raw image data (RGB values) provides a more accurate estimation of the parameters of NLC ice particle size distribution compared to that obtained from the ground. We will estimate the NLC particle size distribution based on the RGB color ratio technique in a future paper.

5. Conclusions

European balloon infrastructure project HEMERA and CNES balloon campaign KLIMAT were conducted in August 2021 at Esrange (northern Sweden). The Stratospheric Observation of Noctilucent Clouds (SONC) balloon-borne experiment was successfully performed onboard the XENON balloon on the night of 16ï 17 August 2021, reaching the maximum altitude of 32.7 km. From the technical point of view we can conclude the following:

1. All three optical cameras and the electronics were completely operational in the stratosphere for about 13 hours at low temperatures of about ï 30°C.
2. Each camera took about 40,000 images during the balloon flight in the stratosphere.
3. The SONC instrument survived and had no damage after the landing of the gondola.

The first scientific results of the SONC experiment are as follows:

1. Two wide-angle cameras registered the extended field of NLC in the twilight sky sector. The NLC were of a moderate brightness and had a rather short lifetime of about 3.3 hours.
2. The NLC field had horizontal scales of about 1700 km stretching from 7°W to 40°E, and about 300 km from 68° to 71°N. It moved as a whole to the south-west, with the average observed speed of ~53 m/s and with the average azimuth of ~236°. It is impossible to observe an NLC at such large horizontal scales of 1700 km from the ground, revealing advantages of measurements from stratospheric heights.
3. The NLC field was modulated by atmospheric gravity waves of various scales: medium-scale gravity waves with horizontal wavelengths of about 24, 34, 51 and 103 km as well as short-lived small-scale waves with a horizontal wavelength of about 11 km. The simultaneous observation of short (11 km) wave scales and the large-scale NLC field at horizontal distances up to 1700 km has been obtained for the first time.
4. Esrange lidar as well as Aura/MLS satellite measurements demonstrated low temperatures of 135ï 142 K (below the frost point temperature of 145ï 148 K) in the mesopause region where the NLC were observed. At the same time, large variability (15ï 20 K) of the temperature around the freezing point did not allow ice particles to grow to large sizes, leading to the formation of small ice particles and, as a result, to weak backscattered signal registered by the lidar at 84 km and 86 km above Esrange.

5. EISCAT radar (Tromsø) and MAARSY (Andøya) have simultaneously registered a presence of PMSE in the same mesopause volume together with the NLC seen from the balloon. The PMSE were located between 83 and 88 km altitudes and were modulated by propagating gravity waves. The simultaneous registration of NLC, observed from the stratosphere, and PMSE in the same volume of the mesopause above northern Scandinavia has been done for the first time.

Data analysis regarding the wave dynamics and NLC ice particle microphysical properties will be presented in future papers.

Acknowledgments

The XENON balloon flight was provided by the French space agency CNES funded by the European Union's Horizon 2020 research and Innovation programme, and received support from the European Commission in the frame of the EU grant agreement 730970-HEMERA. The SONC experiment hardware (the NLC imager and electronic unit) was funded by the Kempe Foundation (Kempestiftelserna, Sweden) under grant agreement JCK-1901.4. Ingrid Mann and Viswanathan Lakshmi Narayanan are supported by the Research Council of Norway project 275503, and their EISCAT observations are supported by the Research Council of Norway project 245683. The authors thank the Aura/MLS team for providing temperature and water vapor data around the globe.

Data availability

Data used in the present paper are available at the HEMERA Data Centre (https://data.hemera-h2020.eu/atmospheric-balloonexperiments/#/) as well as will be made available on request.

References

Bageston, J.V., Wrasse, C.M., Gobbi, D., Takahashi, H., Souza, P.B., 2009. Observation of mesospheric gravity waves at Comandante Ferraz Antarctica Station (62°S). Ann. Geophys. 27, 2593ï 2598.

Bailey, S.M., Thomas, G.E., Rusch, D.W., Merkel, A.W., Jeppesen, C., Carstens, et al., 2009. Phase functions of polar mesospheric cloud ice as observed by the CIPS instrument on the AIM satellite. J. Atmos. Sol. Terr. Phys. 71, 373ï 380. http://dx.doi.org/10.1016/j.jastp.2008.09.039.

Baumgarten, G., Fiedler, J., Fricke, K.H., Gerding, M., Hervig, M., Hoffmann, P., et al., 2009. The noctilucent cloud (NLC) display during the ECOMA/MASS sounding rocket flights on 3 August 2007: morphology on global to local scales. Ann. Geophys. 27, 953ï 965.

Baumgarten, G., 2010. Doppler Rayleigh/Mie/Raman lidar for wind and temperature measurements in the middle atmosphere up to 80 km. Atmos. Meas. Tech. 3, 1509-1518. doi:10.5194/amt-3-1509-2010.

Baumgarten, G., Fritts, D.C., 2014. Quantifying Kelvin-Helmholtz instability dynamics observed in noctilucent clouds: 1. Methods and observations. J. Geophys. Res. Atmos. 119, 9324ï 9337. doi:10.1002/2014JD021832.

Blum, U., Fricke, K.H., 2005. The Bonn University lidar at the Esrange: technical description and capabilities for atmospheric research. Ann. Geophys. 23, 1645ï 1658.

Bronshten, V.A., Grishin, N.I., 1970. Noctilucent clouds. Nauka, Moscow.

Chandran, A., Rusch, D.W., Palo, S.E., Thomas, G.E., and Taylor, M.J., 2009. Gravity wave observations in the summertime polar mesosphere from the Cloud Imaging and Particle Size (CIPS) experiment on the AIM spacecraft, J. Atmos. Sol. Terr. Phys. 71, 392ï 400. doi:10.1016/j.jastp.2008.09.041.

Cho, J.Y.N., Röttger, J., 1997. An updated review of polar mesosphere summer echoes: observations, theory, and their relationship to noctilucent clouds and subvisible aerosols. J. Geophys. Res. 102, 2001ï 2020. https://doi.org/10.1029/96JD02030.

Dalin, P., Pertsev, N., Perminov, V., Efremov, D., Romejko, V., 2020. Stratospheric observations of noctilucent clouds: a new approach in studying middle- and large-scale mesospheric dynamics. Ann. Geophys. 38, 61ï 71. https://doi.org/10.5194/angeo-38-61-2020.

Dalin, P., Pertsev, N., Perminov, V., Efremov, D., Romejko, V., 2019. Looking at ñnight-shiningò clouds from the stratosphere. Eosï AGU 100, https://doi.org/10.1029/2019EO118439.

Dalin, P., Pogoreltsev, A., Pertsev, N., Perminov, V., Shevchuk, N., Dubietis, A., Zalcik, M., et al., 2015. Evidence of the formation of noctilucent clouds due to propagation of an isolated gravity wave caused by a tropospheric occluded front. Geophys. Res. Lett. 42, 2037ï 2046. https://doi.org/10.1002/2014GL062776.

Dalin, P., Connors, M., Schofield, I., Dubietis, A., Pertsev, N., Perminov, V., et al., 2013. First common volume ground-based and space measurements of the mesospheric front in noctilucent clouds. Geophys. Res. Lett. 40, 6399ï 6404. doi:10.1002/2013GL058553.

Dalin, P., Pertsev, N., Frandsen, S., Hansen, O., Andersen, H., Dubietis, A., Balciunas, R., 2010. A case study of the evolution of a Kelvin-Helmholtz wave and turbulence in noctilucent clouds. J. Atmos. Sol. Terr. Phys. 72, 14-15, 1129-1138. doi:10.1016/j.jastp.2010.06.011.

Dalin, P., Pertsev, N., Zadorozhny, A., Connors, M., Schofield, I., Shelton, I., et al., 2008. Ground-based observations of noctilucent clouds with a northern hemisphere network of automated digital cameras. J. Atmos. Sol. Terr. Phys. 70, 1460ï 1472.

DeLand, M.T., Thomas, G.E., 2015. Updated PMC trends derived from SBUV data. J. Geophys. Res. Atmos. 120, 2140-2166. doi:10.1002/2014JD022253.

Demissie, T.D., Espy, P.J., Kleinknecht, N.H., Hatlen, M., Kaifler, N., Baumgarten, G., 2014. Characteristics and sources of gravity waves observed in noctilucent cloud over Norway. Atmos. Chem. Phys. 14, 12133ï 12142. doi:10.5194/acp-14-12133-2014.

Dong, W., Fritts, D.C., Thomas, G.E., Lund, T.S., 2021. Modeling responses of polar mesospheric clouds to gravity wave and instability dynamics and induced large-scale motions. J. Geophys. Res. Atmos. 126, e2021JD034643. https://doi.org/10.1029/2021JD034643.

Dubietis, A., Dalin, P., Balciunas, R., Cernis, K., Pertsev, N., Sukhodoev, V., et al., 2011. Noctilucent clouds: modern ground-based photographic observations by a digital camera network. Applied Optics 50, 28, F72-F79. doi:10.1364/AO.50.000F72.

Fiedler, J., Baumgarten, G., Berger, U., Hoffmann, P., Kaifler, N., Lübken, F.-J., 2011. NLC and the background atmosphere above ALOMAR. Atmos. Chem. Phys. 11, 5701ï 5717. doi:10.5194/acp-11-5701-2011.

Fritts, D.C., Smith, S.A., Balsley, B.B., Philbrick, C.R., 1988. Evidence of gravity wave saturation and local turbulence production in the summer mesosphere and lower thermosphere during the STATE experiment. J. Geophys. Res. 93, D6, 7015-7025.

Fritts, D.C., Isler, J.R., Thomas, G.E., Andreassen, Ø., 1993. Wave breaking signatures in noctilucent clouds. Geophys. Res. Lett. 20, 2039ï 2042. doi:10.1029/93GL01982.

Fritts, D.C., Miller, A.D., Kjellstrand, C.B., Geach, C., Williams, B.P., et al., 2019. PMC Turbo: studying gravity wave and instability dynamics in the summer mesosphere using polar mesospheric cloud imaging and profiling from a stratospheric balloon. J. Geophys. Res. Atmos. 124. https://doi.org/10.1029/2019JD030298.

Fritts, D. C., Baumgarten, G., Wan, K., Werne, J. A., Lund, T., 2014. Quantifying Kelvin-Helmholtz instability dynamics observed in noctilucent clouds: 2. Modeling and interpretation of observations. J. Geophys. Res. Atmos. 119, 9324ï 9337. https://doi.org/10.1002/2014JD021832.

Froidevaux, L., Livesey, N.J., Read, W.G., Jiang, Y.B., Jiménez, C.C., Filipiak, M.J., Schwartz, M.J., et al., 2006. Early validation analyses of atmospheric profiles from EOS MLS on the Aura satellite. IEEE Transactions on Geoscience and Remote Sensing 44, 5, 1106-1121.

Gadsden, M., Schröder, W., 1989. Noctilucent Clouds. Springer, New York.

Ge, S., Li, H., Meng, L., Wang, M., Xu, T., Ullah, S., Rauf, A., Hannachid, A., 2020. On the radar frequency dependence of polar mesosphere summer echoes. Earth and Planetary Physics 4, 571-578. https://doi.org/10.26464/epp2020061.

Gumbel, J., Witt, G., 2001. Rocket-borne photometry of NLC particle populations. Adv. Space Res. 28, 7, 1053-1058.

Haurwitz, B., Fogle, B., 1969. Wave forms in noctilucent clouds. Deepï Sea Research 16, 85-95.

Jensen, E.J., Thomas, G.E., 1994. Numerical simulations of the effects of gravity waves on noctilucent clouds. J. Geophys. Res. Atmos. 99, 3421ï 3430. https://doi.org/10.1029/93JD01736.

Karlsson, B., Gumbel, J., 2005. Challenges in the limb retrieval of noctilucent cloud properties from Odin/OSIRIS. Adv. Space Res. 36, 935-942. doi:10.1016/j.asr.2005.04.074.

Kirkwood, S., Stebel, K., 2003. Influence of planetary waves on noctilucent clouds occurrence over NW Europe. J. Geophys. Res. 108, D8, 8440. doi:10.1029/2002JD002356.

Klostermeyer, J., 1998. A simple model of the ice particle size distribution in noctilucent clouds. J. Geophys. Res. Atmos. 103 (D22), 28 743ï 28 752.

Lambert, A., Read, W.G., Livesey, N.J., Santee, M. L., Manney, G.L., Froidevaux, L., Wu, D.L., Schwartz, M.J., Pumphrey, H.C., Jimenez, C., Nedoluha, G.E., et al., 2007. Validation of the Aura Microwave Limb Sounder middle atmosphere water vapor and nitrous oxide measurements. J. Geophys. Res. 112, D24S36.

Latteck, R., Singer, W., Rapp, M., Vandepeer, B., Renkwitz, T., Zecha, M., Stober, G., 2012. MAARSY - the new MST radar on Andøya-system description and first results. Radio Sci. 47, RS10006. doi:10.1029/2011RS004775.

Liu, X., Yue, J., Xu, J., Yuan, W., Russell III, J.M., Hervig, M. E., Nakamura, T., 2016. Persistent longitudinal variations in 8 years of CIPS/AIM polar mesospheric clouds. J. Geophys. Res. Atmos. 121, 8390ï 8409. doi:10.1002/2015JD024624.

Ludlam, F.H., 1957. Noctilucent clouds. Tellus IX, 3, 341-364.

Mann, I., Gunnarsdottir, T., Häggström, I., Eren, S., Tjulin, A., Myrvang, M., Rietveld, M., Dalin, P., Jozwicki, D., Trollvik, H., 2019. Radar studies of ionospheric dust ï plasma phenomena. Contributions to Plasma Physics, 59:e201900005. https://doi.org/10.1002/ctpp.201900005.

Mann, I., Häggström, I., Tjulin, A., Rostami, S., Anyairo, C.C., Dalin, P., 2016. First wind shear observation in PMSE with the tristatic EISCAT VHF radar. J. Geophys. Res. Space Phys. 121(11), 2169-9380. https://doi.org/10.1002/2016JA023080.

McClintock, W., Rusch, D.W., Thomas, G.E., Merkel, A.W., Lankton, M.R., Drake, V.A., Bailey, S.M., Russell III, J.M., 2009. The cloud imaging and particle size experiment on the aeronomy of ice in the mesosphere mission: instrument concept, design, calibration, and on-orbit performance. J. Atmos. Sol. Terr. Phys. 71. http://dx.doi.org/10.1016/j.jastp.2008.10.011.

Miller, A.D., Fritts, D.C., Chapman, D., Jones, G., Limon, M., Araujo, D., et al, 2015. Stratospheric imaging of polar mesospheric clouds: a new window on small-scale atmospheric dynamics. Geophys. Res. Lett. 42, 6058ï 6065. doi:10.1002/2015GL064758.

Murphy, D.M., Koop, T., 2005. Review of the vapour pressures of ice and supercooled water for atmospheric applications. Q. J. R. Meteorol. Soc. 131, 1539ï 1565. doi:10.1256/qj.04.94.

Narayanan, V.L., Häggström, I., Mann, I., 2022. Effects of particle precipitation on the polar mesospheric summer echoes observed by EISCAT VHF 224 MHz radar. Adv. Space Res. 69, 3350ï 3361. doi: 10.1016/j.asr.2022.02.015.

Pautet, P.-D., Stegman, J., Wrasse, C.M., Nielsen, K., Takahashi, H., Taylor, M.J., et al., 2011. Analysis of gravity waves structures visible in noctilucent cloud images. J. Atmos. Sol. Terr. Phys. 73, 14-15, 2082-2090. doi: 10.1016/j.jastp.2010.06.001.

Pertsev, N., Dalin, P., Perminov, V., 2015. Influence of semidiurnal and semimonthly lunar tides on the mesopause as observed in hydroxyl layer and noctilucent clouds characteristics. Geomagn. Aeron. 55, 6, 811ï 820. doi:10.1134/S0016793215060109.

Rapp, M., Lübken, F.-J., Müllemann, A., Thomas, G., Jensen, E., 2002. Small scale temperature variations in the vicinity of NLC: experimental and model results. J. Geophys. Res. 107, D19, 4392. doi:10.1029/2001JD001241.

Rapp, M., Lübken, F.-J., 2003. On the nature of PMSE: electron diffusion in the vicinity of charged particles revisited. J. Geophys. Res. 108D8, 8437. https://doi.org/10.1029/2002JD002857.

Read, W.G., Lambert, A., Bacmeister, J., Cofield, R.E., Christensen, L.E., Cuddy, D.T., Daffer, W.H., Drouin, B.J., Fetzer, E., Froidevaux, et al., 2007. Aura Microwave Limb

Sounder upper tropospheric and lower stratospheric H2O and relative humidity with respect to ice validation. J. Geophys. Res. 112, D24S35.

Reimuller, J.D., Thayer, J.P., Baumgarten, G., Chandran, A., Hulley, B., Rusch, D., Nielsen, K., Lumpe, J., 2011. Synchronized imagery of noctilucent clouds at the day-night terminator using airborne and spaceborne platforms. J. Atmos. Sol. Terr. Phys. 73, 14-15, 2091-2096.

Russell III, J.M., Bailey, S.M., Gordley, L.L., Rusch, D.W., Horányi, M., Hervig, M.E., Thomas, G.E., Randall, C.E., Siskind, D.E., Stevens, M.H., Summers, M.E., Taylor, M.J., Englert, C.R., Espy, P.J., McClintock, W.E., Merkel, A.W., 2009. Aeronomy of Ice in the Mesosphere (AIM): overview and early science results. J. Atmos. Sol. Terr. Phys. 71 (3-4), 289-299. http://dx.doi.org/10.1016/j.jastp.2008.08.011.

Schwartz, M.J., Lambert, A., Manney, G.L., Read, W.G., Livesey, N.J., Froidevaux, L., Ao, C.O., Bernath, P.F., Boone, C.D., Cofield, R.E., et al., 2008. Validation of the Aura Microwave Limb Sounder temperature and geopotential height measurements. J. Geophys. Res. 113, D15S11.

Shevchuk, N., Pertsev, N., Dalin, P., Perminov, V., 2020. Wave-induced variations in noctilucent cloud brightness: model and experimental studies. J. Atmos. Sol. Terr. Phys. 203, 105257, https://doi.org/10.1016/j.jastp.2020.105257.

Suzuki, H., Matsumoto, A., Dalin, P., Nakamura, Y., Ishii, S., Sakanoi, K., Sakaguchi, K., Takada, T., Tsuda, T.T., Hozumi, Y., 2022. Capability of airline jets as an observation platform for noctilucent clouds at middle latitudes. Progress in Earth and Planetary Science 9, 11. https://doi.org/10.1186/s40645-022-00469-4.

Taylor, M.J., Pautet, P.-D., Zhao,Y., Randall, C.E., Lumpe, J., Bailey, S.M., et al., 2011. High-latitude gravity wave measurements in noctilucent clouds and polar mesospheric clouds. In: Abdu M., Pancheva, D. (eds), Aeronomy of the Earth's Atmosphere and Ionosphere, IAGA Special Sopron Book Series, Springer, Dordrecht, 2, 93-105, doi:10.1007/978-94-007-0326-1_7.

Thomas, G.E.: Solar Mesosphere Explorer measurements of polar mesospheric clouds (noctilucent clouds), J. Atmos. Terr. Phys., 46, 9, 819-824, 1984.

Thurairajah, B., Cullens, C.Y., Bailey, S.M., 2021. Characteristics of a mesospheric front observed in polar mesospheric cloud fields. J. Atmos. Sol. Terr. Phys. 218, 105627, https://doi.org/10.1016/j.jastp.2021.105627.

Turco, R.P., Toon, O.B., Whitten, R.C., Keesee, R.G., Hollenbach, D., 1982. Noctilucent clouds: simulation studies of their genesis, properties and global influences. Planet. Space Sci. 30 (11), 1147ï 1181.

Ugolnikov, O.S., 2021. Altitude and particle size measurements of noctilucent clouds by RGB photometry: radiative transfer and correlation analysis.https://arxiv.org/abs/2112.03895.

Ugolnikov, O.S., Galkin, A.A., Pilgaev, S.V., Roldugin, A.V., 2017. Noctilucent cloud particle size determination based on multi-wavelength all-sky analysis. Planet. Space Sci. 146, 10-19. https://doi.org/10.1016/j.pss.2017.08.006.

Von Cossart, G., Fiedler, J., von Zahn, U., 1999. Size distributions of NLC particles as determined from 3-color observations of NLC by ground-based lidar. Geophys. Res. Lett. 26, 1513-1516.

Witt, G., 1962. Height, structure and displacements of noctilucent clouds. Tellus XIV, 1, 1ï 18.

Zadorozhny, A.M., Tyutin, A.A., Witt, G., Wilhelm, N., Wälchli, U., Cho, J.Y.N., Swartz, W.E., 1993. Electric field measurements in the vicinity of noctilucent clouds and PMSE. Geophys. Res. Lett. 20, 20, 2299-2302.

Figure captions:

Figure 1. The SONC instrument is composed of three SONY Ŭ7 Mark III cameras and the electronic unit (the grey box with the red button), which was used for observing noctilucent clouds on the XENON stratospheric balloon on the night 16-17 August 2021. Two cameras are equipped with wide-angle lenses and one camera has a narrow-angle lens (located in between two wide-angle cameras).

Figure 2. (Left) The XENON balloon height profile on the night 16-17 August 2021. (Right) The horizontal trajectory of the XENON flight. The red dot marks the position of the balloon launch at Esrange. The vertical and horizontal arrows indicate horizontal scales in km. The red and green asterisks on the both panels indicate the start and end of the SONC experiment operation, respectively.

Figure 3. Noctilucent clouds observed from the stratosphere during the SONC balloon-borne experiment on the night 16-17 August 2021. Examples of images of noctilucent clouds taken by two wide-angle cameras of the SONC experiment from the stratosphere at about 32.5 km: Left-panel images were taken at 23:45:41, 23:55:41, 00:05:41 UT by the left wide-angle camera (see Figure 1), pointing to 278° from the north. Middle-panel images were taken at 22:37:13, 22:47:13, 22:57:13 UT by the left wide-angle camera, pointing to 20°. Right-panel images were taken at 22:04:02, 22:14:02, 22:24:07 UT by the right wide-angle camera, pointing to 38° from the north. For the geometry of the cameras the reader is refer to Figure 1.

Figure 4. The upper panel is the enlarged part of Figure 3c. The lower panel is the enlarged part of Figure 3g. The dots and corresponding numbers mark gravity wave crests and their horizontal wavelengths in km being analyzed in the paper.

Figure 5. Projection of the images shown in Figure 3 on the Earthôs surface. When projected on the surface, the mean NLC altitude was equal to 85 km. The black asterisk, the magenta square and the yellow dot show the positions of Esrange, Andøya and Tromsø, respectively.

Figure 6. (Left) The lidar count profile integrated over 2 hours from 22:30 UT to 00:30 UT on the night 16-17 August 2021. Two small peaks in the profile which might be attributed to NLC layers are marked with the red arrows. (Right) Temperatures profiles as measured by Aura/MLS spectrometer: the magenta profile is to the north-east of Esrange measured at

00:45 UT, the red profile is to the north-west of Esrange measured at 02:24 UT, the green profile is the Aura frost point temperature estimated from water vapor measurements. The blue profile is the mean Esrange lidar temperature as estimated from the lidar count profile and the blue horizontal bars show uncertainties (1 standard deviation) of the mean temperature profile.

Figure 7. A map of the difference between Aura/MLS temperature and the frost point temperature at about 90 km altitude on 17 August 2021. The blue color code (negative values) means the temperature is below the frost point temperature allowing the existence of ice particles. The red oval shows the location of the NLC field as observed from the stratosphere. The black asterisk, the magenta square and the yellow dot show the positions of Esrange, Andøya and Tromsø, respectively.

Figure 8. MAARSY 53 MHz measurements of PMSE volume reflectivity above Andøya (69.30°N; 16.04°E) during the SONC balloon experiment on the night 16-17 August 2021. Two red arrows show the beginning and end of the NLC observation from the stratosphere.

Figure 9. EISCAT 224MHz radar measurements of PMSE parameters above Tromsø (69.58°N; 19.23°E) during the SONC balloon experiment on the night 16-17 August 2021. The upper panel shows the radar power, the middle panel is the Doppler shift and the lower panel illustrates the radar spectral width. Two red arrows show the beginning and end of the NLC observation from the stratosphere.

Table 1. Technical characteristics of the SONC imager composed of two wide-angle Sony Ŭ7 Mark III cameras and one narrow-angle Sony Ŭ7 Mark III camera.

	Field of view and focal length	Sensor type and size, pixels	Bit depth, image format	Spatial resolution at 83 km as seen from 33 km at 35° elevation angle
Wide-angle camera	105.4° x 81.8° 14 mm	CMOS 6000 x 4000	14 raw	63 m
Narrow-angle camera	15.0° x 10.1° 135 mm	CMOS 6000 x 4000	14 raw	6 m